Journal of Nuclear Materials 494 (2017) 182–191

Contents lists available at ScienceDirect

Journal of Nuclear Materials

journal homepage: www.elsevier.com/locate/jnucmat

Finite-element model to predict roll-separation force and defects during rolling of U-10Mo alloys

Ayoub Soulami*, Douglas E. Burkes, Vineet V. Joshi, Curt A. Lavender, Dean Paxton

Pacific Northwest National Laboratory (PNNL), 902 Battelle Boulevard, P.O. Box 999, Richland, WA 99352, USA

ARTICLE INFO

Article history:
Received 12 July 2016
Received in revised form
30 June 2017
Accepted 3 July 2017
Available online 4 July 2017

Keywords:
Hot rolling
U-10Mo
Finite element
Roll-separation force
Rolling defects
Waviness
Dog-boning

ABSTRACT

A major goal of the Convert Program of the U.S. Department of Energy's National Nuclear Security Administration (DOE/NNSA) is to enable high-performance research reactors to operate with low-enriched uranium rather than the high-enriched uranium currently used. To this end, uranium alloyed with 10 wt% molybdenum (U-10Mo) represents an ideal candidate because of its stable gamma phase, low neutron caption cross section, acceptable swelling response, and predictable irradiation behavior. However, because of the complexities of the fuel design and the need for rolled monolithic U-10Mo foils, new developments in processing and fabrication are necessary. This study used a finite-element code, LS-DYNA, as a predictive tool to optimize the rolling process. Simulations of the hot rolling of U-10Mo coupons encapsulated in low-carbon steel were conducted following two different schedules. Model predictions of the roll-separation force and roll pack thicknesses at different stages of the rolling process were compared with experimental measurements. The study reported here discussed various attributes of the rolled coupons revealed by the model (e.g., waviness and thickness non-uniformity like dog-boning). To investigate the influence of the cladding material on these rolling defects, other cases were simulated: hot rolling with alternative can materials, namely, 304 stainless steel and Zircaloy-2, and bare-rolling. Simulation results demonstrated that reducing the mismatch in strength between the coupon and can material improves the quality of the rolled sheet. Bare-rolling simulation results showed a defect-free rolled coupon. The finite-element model developed and presented in this study can be used to conduct parametric studies of several process parameters (e.g., rolling speed, roll diameter, can material, and reduction).

1. Introduction

Transition from high-enriched uranium (HEU) fuel to low-enriched uranium (LEU) fuel in research and test reactors has been a global focus for the past three decades [1]. The U.S. Department of Energy/National Nuclear Security Administration's (DOE/NNSA's) Convert Program is considering uranium alloyed with nominally 10 wt% molybdenum (U-10Mo) as a high density, LEU fuel that has the potential to enable the conversion of high-performance research and test reactors from the use of HEU fuel to LEU fuel. In U-10Mo, the molybdenum in the uranium stabilizes the cubic gamma phase allowing for acceptable irradiation and swelling behavior under irradiation [2–5]. A monolithic U-10Mo foil clad in Zirconium alloy and encapsulated in aluminum alloy possesses the greatest possible uranium density in the fuel region, maintains excellent resistance to anisotropic growth (i.e., swelling), and is compatible with existing reactor designs [6]. In addition, the U-10Mo fuel alloy represents a good combination of irradiation performance, oxidation resistance, strength, and ductility. Therefore, it is ideal for reducing nuclear proliferation risks associated with the transportation and storage of large quantities of HEU. However, little literature is available to model the processing of this alloy and the development of a capability to predict the defects formed therein.

When designing hot-rolling schedules, particularly for roll packs, the ability to quickly investigate the influence of process variables on properties (e.g., roll-separation force) is highly desirable. Understanding these properties is important for procuring the right equipment (in this case the rolling mill), optimizing the process efficiency, achieving desired foil quality, engineering the

* Corresponding author.
E-mail addresses: ayoub.soulami@pnnl.gov, ayoub.soulami@gmail.com (A. Soulami).

http://dx.doi.org/10.1016/j.jnucmat.2017.07.006
0022-3115/

Table 1
Physical dimensions (mm) of the alloy coupon and roll pack used in the current study.

Alloy Coupon	Thickness	2.72
	Width	18.6
	Length	29.5
Roll pack	Thickness	9.40
	Width	37.7
	Length	48.5

desired foil characteristics, and developing reasonable production schedules on a rational scientific basis. Finite-element modeling (FEM) is an important tool for reducing costs and improving production efficiencies related to industrial-process development and optimization, particularly because of the complexity of handling radioactive materials. Ozaltun et al. [5] used FEM to investigate the residual stresses in monolithic U-10Mo alloy plates during hot-isostatic pressing. Other researchers used FEM to simulate the rolling process in non-uranium materials. Kong et al. [7] investigated the effects of temperature, rolling velocity and reduction on the strain rate distribution, the deformation and rolling force during the rolling of Zirconium plates using a simplified implicit stress-updating algorithm in Abaqus. Hwu and Lenard [8] used a FEM formulation to simulate a flat-rolling process to investigate the effects of work-roll distortion and various friction conditions on the strain distribution within the rolled sheet. Nepershin [9] developed a plane strain FEM model for a hot-rolling process, in which sticking friction is assumed between the work-roll and deforming material. Shuai et al. used FEM to investigate rolling force and torque during a titanium alloy bar-rolling process [10]. Tieu et al. [11] used a three-dimensional rigid-viscoplastic FEM model to simulate the hot rolling of strip to investigate the friction variation in the roll bite and the effect of lubrication in hot-strip rolling on roll-separation force. Knight et al. [12] used FEM to study the influence of roll-speed mismatch on strip curvature during the roughing stages of a hot-rolling mill.

In this paper, we investigated the effects of U-10Mo alloy rolling on the rolls separation force, and performed several process optimizations to avoid any defects formed during rolling. A finite-element model of the rolls and roll pack was developed using the commercial code LS-DYNA© [13]. The model was first validated through comparison with actual rolling data, and then used to perform various parametric studies investigating the effect of can material on the rolled sheet defects. This modeling tool can be used by fuel manufacturers to design their rolling schedules and select the appropriate equipment (in terms of rolling mill diameter). Foundation of this work and a parametric study using the FEM model can be found in reports [14] and [15].

2. Finite-element model

2.1. Model description and geometry

The present study used explicit solver in LS-DYNA to simulate the hot rolling of LEU fuel foils. Coupled thermal-structural analysis, using elastic-plastic-thermal constitutive equations, was adopted to describe the material behavior. To exploit the symmetry of the geometry of the roll pack and the rolls, only half of the setup was modeled. The symmetry plane was chosen to be the mid-plane, cutting the roll pack in half lengthwise and, to account for the symmetry, appropriate boundary conditions were applied. This model was also used to simulate the rolling of non-symmetrical coupons with respect to the plan between the rollers. Therefore, only half-symmetry is considered. The rolling setup consisted of two rolls and a roll pack made up of a coupon and the can material. Rolls were 254 mm in diameter and 254 mm wide and were considered rigid and non-distorting. Table 1 summarizes the dimensions of the alloy coupon and roll pack. The model is using the geometry of an actual coupon which was rolled experimentally and its data used to validate the simulation results. Rolling simulations for different rolls and coupons geometries were also conducted and results presented in Ref. [15]. Although the coupon length effect is an important aspect to take into consideration in rolling simulations, it does not affect the roll separating force which depends on the coupon's width, roll diameter, and reduction.

The rolls were modeled using 51072 rigid shell elements (for the half model); with an initial mesh size of ~2 × 2 mm. The roll pack was modeled using three-dimensional (3D) 69649 brick elements that had an initial mesh size of ~0.5 × 0.5 × 0.5 mm. Fully integrated quadratic 8 node elements with nodal rotations were selected in LS-Dyna and convergence study conducted on the element size.

Fig. 1 represents the roll pack as modeled in LS-DYNA. The actual roll assembly is welded along the perimeter to form the can. In the model, the welded region was considered to have the same mechanical properties as the parent can material. However, to account for the weld, the outer layer of elements in contact with the top cover, picture frame, and bottom cover of the can were tied to each

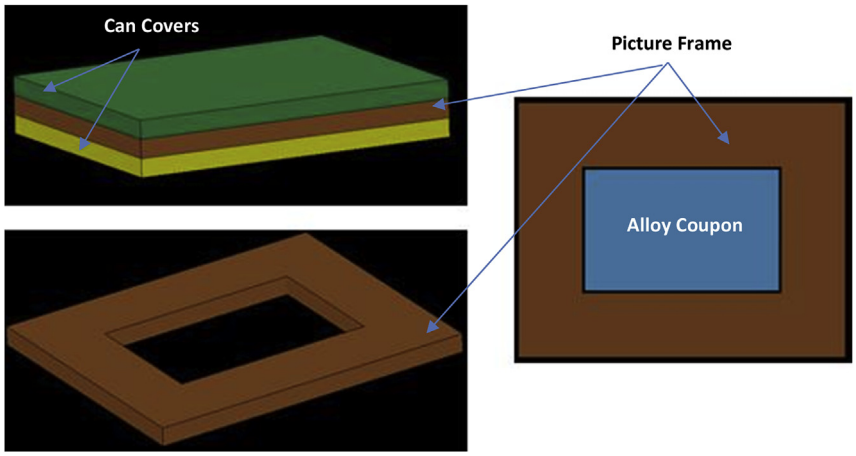

Fig. 1. Representation of the full roll pack. The blue area represents the alloy coupon, the green area is the top cover of the can, the yellow area is the bottom cover of the can, and the brown area is the frame. (For interpretation of the references to colour in this figure legend, the reader is referred to the web version of this article.)

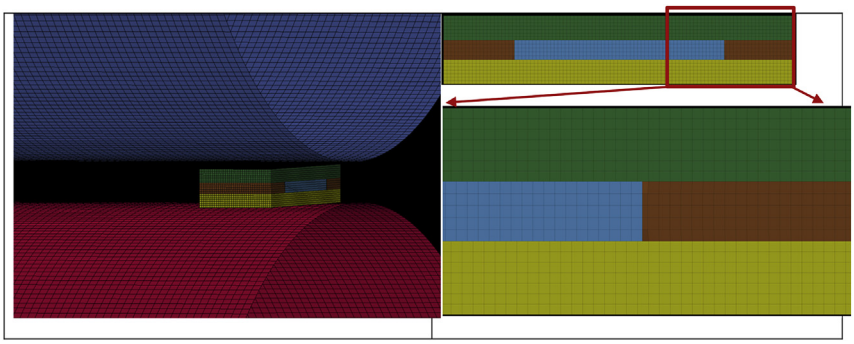

Fig. 2. Different views of the FEM model (half).

other. For this purpose, the coincident nodes of these elements have been merged.

Fig. 2 shows different views of the half model. The roll pack is shown at the entrance in between the rolls.

Several contact cards were tested and "*AUTOMATIC_SURFACE_TO_SURFACE_THERMAL" with a friction coefficient of 0.35 between the rolls and the can was selected from the contact cards library in LS-Dyna. This card defines the contact and the temperature exchange between the roll pack and the rolls. Appropriate mechanical properties will be applied during the simulation on each element as a function of its temperature. In fact, the model only takes into account the temperature loss due to contact between the roll pack and the rolls. Initial temperature, which is considered uniform on all the nodes, is applied to the roll pack at the beginning of every pass. This temperature is calculated taking into account the temperature loss due to radiation with the surrounding air during the transfer from the exit of the rolls to the entrance of the rolls, or from the furnace into the entrance of the rolls when re-heats are necessary. While the rolls are considered to be rigid material, the can (low-carbon steel, AISI 1018) and the alloy coupon (U-10Mo) were modeled using the *MAT_ELASTIC_PLASTIC_THERMAL material card in LS-DYNA. This constitutive model is temperature-dependent and suited to model isotropic plasticity at high temperatures. This elastic-plastic model is computationally efficient and only needs a few parameters. The difference between yield stress (YS) and the ultimate tensile stress (UTS) with strain were used to determine the plastic hardening moduli of the material.

A rotation velocity of 10 revolutions per minute (rpm) was assigned to the rolls, which corresponds to 1.047 radians per second (rad/s). This equates to a translational velocity of 133 mm/s at the entrance of the rolls. This velocity was applied to the roll pack using the card *INITIAL_VEELOCITY in LS-DYNA. Once a roll pack exits the rolls after a pass, the simulation stops and a restart file is created. This restart file is used to map the deformations, stresses, and temperatures on the roll pack before simulating the next pass. Note that the model will automatically update the material properties for the U-10Mo and steel can based on the actual temperature of the roll pack. Rolls rotation sense and linear velocity direction are flipped so the roll pack enters the rolls for the next pass with the desired reduction rate from the opposite side of the rolls. These steps are repeated for each pass until completion of the desired schedule.

2.2. Temperature boundary

Temperature is critical for determining the material properties of the alloy coupon and the can, particularly because multiple passes are made between reheating. Temperature loss from the roll pack is considered to result from heat conduction from the roll pack to the work rolls and from radiation of the roll pack to the ambient surrounding. Temperature loss can also occur via convection. However, given the rapid transfer times (<10 s) and the difficulty in calculation, temperature loss due to convection was not considered here.

The present model implements temperature loss through radiation boundary conditions and within the contact definition to account for the heat conduction between the roll pack and the rolls. Rolls are heated to an initial temperature of 50 °C whereas the surrounding ambient temperature is 25 °C. To simulate the temperature loss during the transfer of the roll pack from the furnace/exit rolls into the rolls entrance, steps to simulate radiation heat transfer are necessary. During these steps, between every two passes, only heat loss due to radiation with ambient surrounding is considered. To optimize computation time, and using data from the experiments, an average temperature loss is calculated and applied to the roll pack as an initial temperature boundary condition after every pass. This temperature loss is time-dependent (i.e., the time required for the catcher to pass the roll pack-back to the pitcher). The temperature loss, ΔT_R, is determined using Equation (1) following the process described by Seredynski [16].

$$\Delta T_r = \frac{2\psi\xi}{\rho c h_m} T^4 \Delta t \tag{1}$$

Where ψ is the Stefan-Boltzmann constant (5.670367×10^{-8} kg s^{-3} K^{-4}), ξ is the emissivity (unitless) of the roll pack (oxidized), T (Kelvin) is the temperature of the roll pack prior to exiting the furnace or upon exiting the rolls, ρc is the temperature-dependent volumetric heat capacity (J/m^{3}K) of the roll pack, Δt is the elapsed time (seconds) between removal from the furnace or work rolls and insertion of the roll pack into the work rolls, and h_m (meters) is the thickness of the roll pack prior to the reduction pass. Equation (1) is based on three basic assumptions: (i) the ambient temperature is neglected (i.e., $T \gg T_a$), (ii) the geometry of the roll pack represents a plate (i.e., $b_m \gg h_m$ and $l \gg h_m$), and (iii) short time intervals are considered (i.e., $\Delta t < 20$ s). All three assumptions are valid for our application. In addition, heat gain due to plastic deformation is modeled during deformation, even though the temperature rise is not very significant compared to the rolling temperature. This equation was used to establish the initial boundary condition of the roll pack at the entrance of the rolls at every pass. The temperature loss occurs either during the transfer

from the furnace to the rolls, or between the exit and the entrance of the rolls when no reheat is taking place between passes.

2.3. Determination of defects during the rolling process

Non-uniformity of thickness is one of the most common issues associated with rolling. Thickness variation could be present along the length of the rolled strip as well as across the width. Longitudinal changes in thickness are caused by variations in incoming thickness, friction, hardness, temperature, etc. along the rolled strip. Variations in these factors are even more pronounced in the case of coupons encapsulated in cans composed of a picture frame and top and bottom covers as shown in Fig. 1. This configuration causes variations in roll-separation force and thus variation in the thickness that is proportional to the pressure applied on the rolled sheet-pack. Variations in thickness across the width are generally caused by roll flattening and roll bending under load [17]. This variation can also be caused by the geometry of the roll pack with a significant mismatch of strength between the middle area where the coupon is located and near the edges of the picture frame where only can material is present.

The second geometric non-uniformity considered in this study is "dog-boning." This end effect refers to a localized thickening of the fuel alloy and thinning of the cladding at the edges of the fuel core. In the case of aluminum clad material, dog-boning was demonstrated to be a result of the marked difference in plasticity between the high-uranium core alloy and the aluminum containment materials at the elevated temperature required for rolling [18]. Pedrosa et al. [19] observed dog-boning and delamination at both ends of the samples during the hot co-rolling of U-10Mo with Zircalloy-4 cladding. Pasqualini [20] presented a study in which they showed very little dog-boning while hot rolling a U-10Mo coupon inside a Zirconium can. This is in accordance with the theory that less difference in strength between the core material and the cladding material leads to more uniform deformation.

Waviness of the rolled sheet-pack is also a parameter of utmost interest to rolling engineers, because it often becomes critical for the acceptance or rejection of the rolled flat products. This defect can be caused by various aspects of the rolling process such as bending of the rolls and changes in the roll-separation force along the sheet-pack. Waviness can also be a consequence of dog-boning and a possible gap between the core coupon and the picture frame. Simulations conducted in the current work revealed waviness and dog-boning, which are discussed further in the following sections.

2.4. Material properties

Thermo-physical properties and alloy-preparation methods of U-10Mo have been studied in detail by Burkes et al. [21,22] Joshi et al. [23,24] investigated U-10Mo behavior when it was compression tested at various strain rates and temperatures. They also studied the effect of homogenization on the mechanical properties of U-10Mo. In the absence of actual measurements of the roll pack temperature during experiments, temperature calculations were carried out based on previously developed analytical methods [25]. Those temperatures were used in the current study to apply the appropriate temperature boundary conditions of the roll pack at every pass and select the mechanical properties as an input to the finite-element model. Anisotropy was not included in the simulations. Microstructural observations show banded microstructure after rolling the samples, however the recrystallization that takes place during re-heats anneal the material and equi-axed grains are produced. The aim of this modeling work is to present a modeling approach simple enough to allow for multi-passes rolling simulations with restarts after every pass. The

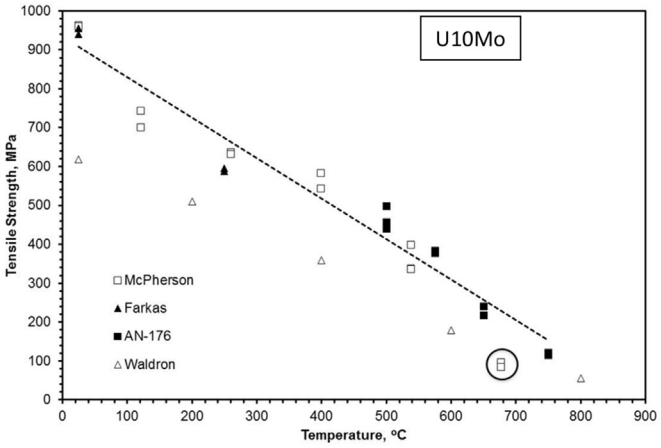

Fig. 3. Temperature-dependent tensile strength data for the U-10Mo alloy. Solid and open shapes represent YS and UTS, respectively.

authors are aware of the complexity of the microstructural features occurring during the hot rolling and therefore adequate assumptions were made neglecting anisotropy which should not significantly affect the predicted roll separating forces or macroscopic non uniformity of the rolled strips.

Four rolling scenarios are considered in the present work: i) rolling of a U-10Mo coupon in a 1018 low-carbon steel can, ii) rolling of a U-10Mo coupon in a 304 Stainless Steel can, iii) rolling of a U-10Mo coupon in a Zircaloy-2 can, and iv) rolling of a U-10Mo coupon with no can material (termed "bare rolling.)" Model input included temperature-dependent tensile properties of U-10Mo, low-carbon steel AISI 1018, 304 stainless steel, and Zircaloy-2. Fig. 3 provides tensile strength as a function of temperature for U-10Mo from various sources [26–29]. A linear best-fit correlation through selected data (Equation (2)) is assumed to represent the temperature-dependent tensile strength of a U-10Mo alloy from room temperature up to 750 °C.

$$\sigma_{y,\mathrm{U-10Mo}}(T) = 933.7 - 1.041T \tag{2}$$

where $\sigma_{y,U-10Mo}$ represents the yield stress in MPa and T the temperature in degrees Celsius.

Peterson and Vandervoort [30] stated that U-10Mo does not undergo work-hardening during deformation in this temperature range. This trend was observed in many tensile data reported in

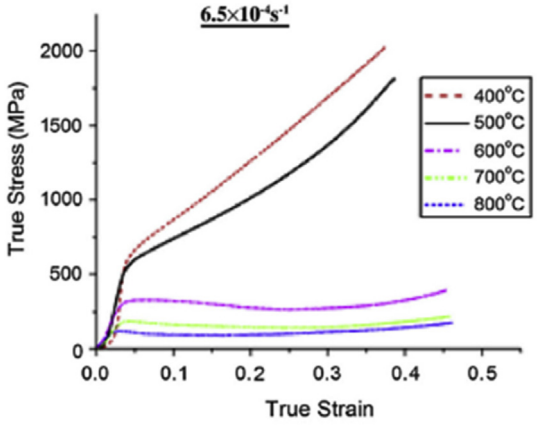

Fig. 4. Stress-strain curves for U-10Mo compression tested at different temperatures [20].

Table 2
Thermo-mechanical properties of U-10Mo, AISI 1018, and Zircaloy-2 [5,21,31–35].

AISI 1018	
Young Modulus	200,000 MPa
Poisson's Ratio	0.3
Density	7800 kg/m^3
Thermal Conductivity	51.9 W/m·°C
Heat Capacity	486 J/kg·°C
Coefficient of Thermal Expansion	14.0 × 10^{-6} m/m·°C
304 Stainless Steel	
Young Modulus	200,000 MPa
Poisson's Ratio	0.33
Density	7800 kg/m^3
Thermal Conductivity	15.5 W/m·°C
Heat Capacity	500 J/kg·°C
Coefficient of Thermal Expansion	17.5 × 10^{-6} m/m·°C
Zircaloy-2	
Young Modulus	96,526 MPa
Poisson's Ratio	0.4
Density	6530 kg/m^3
Thermal Conductivity	21.5 W/m·°C
Heat Capacity	285 J/kg·°C
Coefficient of Thermal Expansion	6.5 × 10^{-6} m/m·°C
U-10Mo	
Young Modulus	65,000 MPa
Poisson's Ratio	0.35
Density	16,060 kg/m^3
Thermal Conductivity	35.5 W/m·°C
Heat Capacity	167 J/kg·°C
Coefficient of Thermal Expansion	16.4 × 10^{-6} m/m·°C

several reports from the 1960s. However, compression tests, done at Pacific Northwest National Laboratory (PNNL) and reported by Joshi et al. [23,24], show that at a particular strain rate, compression samples that were tested below the eutectoid temperature (550 °C) showed significantly higher yield stress and flow stress compared to those that were compression tested above the eutectoid temperature by over 50%. In other words, significant work-hardening is present at temperatures below (550 °C). Fig. 4 represents the true stress-strain curves at different temperatures for U-10Mo tested under compression.

All other thermo-mechanical parameters used as an input to the model are summarized in Table 2. Note that these parameters are considered constant with respect to temperature in the 400–650 °C range. Based upon the studies of Peterson and Vandervoort [30] and Joshi et al. [23,24], two cases were considered for U-10Mo input parameters: (i) no work-hardening and (ii) work-hardening for temperatures below 550 °C. For AISI 1018, 304 stainless steel, and Zircaloy-2, temperature dependent elastic-plastic constitutive models were adopted with tangent modulus to account for the work-hardening present during deformation. Details about the mechanical properties of the cans at various temperatures can be found in Soulami et al. [14].

3. Experimental rolling

Data from experiments involving two different rolling schedules for small alloy coupons were used to validate the model predictions. Details about the rolling procedure are reported in detail in Moore and Marshall [36]. Each rolling schedule used 15 passes; however, the reduction per pass and reheating schedules varied (see Table 3). The first rolling schedule (Schedule A) involved fewer reheating cycles, more subsequent roll passes between reheats, larger reduction rates per pass early in the schedule, and less time to complete. The second rolling schedule (Schedule B) involved many more reheats, fewer subsequent roll passes between reheats, relatively larger reduction rates per pass late in the schedule, and more time to complete.

Table 3 summarizes the reduction rates and roller settings used in Schedules A and B for the first 15 passes.

4. Results and discussion

4.1. Simulated roll-separation force

Simulations were carried out following Schedules A and B using U-10Mo material properties and no work-hardening at high temperatures. Fifteen passes were simulated with a restart and modification of the roll settings and rotation direction between every two passes. The roll-separation force after each pass was calculated from the model and values were compared to experimental measurements (Figs. 5 and 6 for Schedules A and B, respectively). Figs. 5 and 6 both include a predicted entry temperature of the roll pack, which takes into account the radiation with the ambient surroundings, conduction due to contact of the rolls, and an assumed temperature loss of 15 °C to radiation. The temperature is an average value at the cross section of the roll pack in the middle of the rolling reduction.

For both Schedules A and B, the model prediction is in very good agreement with the experimental measurements. For Schedule A, the predicted forces deviate less than 7% over the entire rolling schedule. For Schedule B, a slight divergence appears after Pass 6;

Table 3
Reduction rates, roller settings, and reheats for Schedules A and B.

Pass	Schedule A			Schedule B		
	Reduction Rate	Roll Separating Force (N)	Reheats (°C)	Reduction Rate	Roll Separating Force (N)	Reheats (°C)
0		0	650		0	635
1	10%	136,631		4.32%	44,318	–
2	10%	185,001		4.52%	72,462	640
3	10%	223,024		4.73%	83,733	–
4	7%	213,091		4.97%	112,255	639
5	7%	218,518	629	5.23%	100,049	–
6	7%	150,759		5.52%	132,762	639
7	6%	147,836		5.84%	106,722	–
8	6%	165,060		6.20%	134,745	639
9	6%	175,104		6.61%	128,300	–
10	5%	175,393	617	7.08%	146,475	639
11	5%	133,967		7.62%	128,149	–
12	5%	135,043		8.25%	150,781	639
13	5%	144,931		8.99%	142,806	–
14	5%	160,140		9.88%	167,155	640
15	5%	163,191	591	4.32%	145,537	–

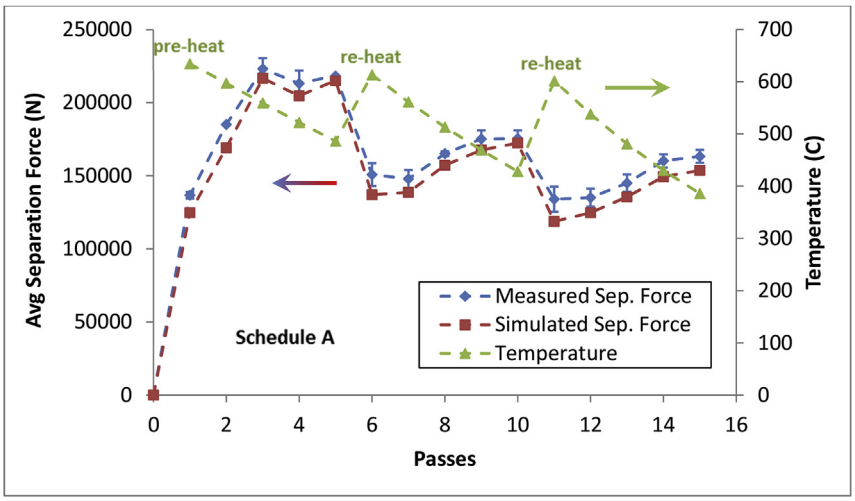

Fig. 5. Measured separation forces compared to simulated separation forces for the first 15 passes of Schedule A.

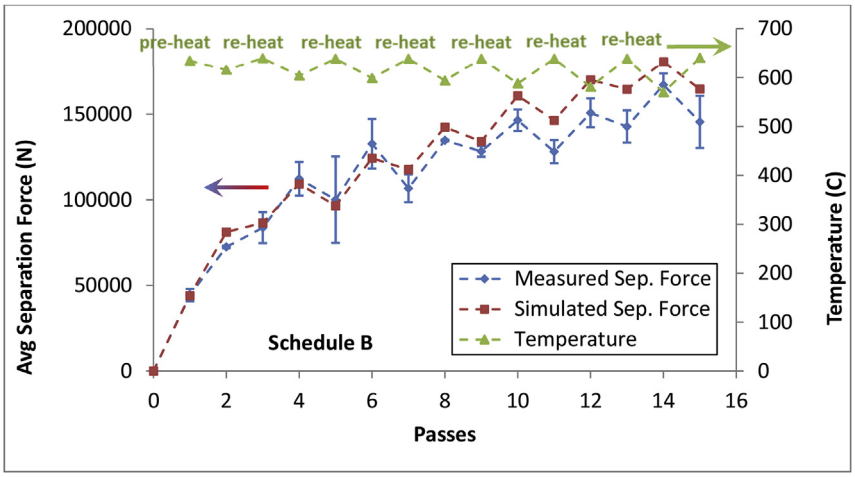

Fig. 6. Measured separation forces compared to simulated separation forces for the first 15 passes of Schedule B.

the deviation (an overprediction of force) reaches a maximum (14%) at the last pass. Given that the forces in the early passes for Schedule B are in close agreement, this divergence may be related to a change in the U-10Mo or 1018 microstructure resulting in a decreased flow stress not accounted for in the U-10Mo or 1018 constitutive relation. This deviation may be more likely in Schedule B where longer times at elevated temperature could have resulted in microstructural changes (e.g., homogenization of any second phases or recrystallization). There is also difference in temperature loss for Schedule A compared to Schedule B; about 250 °C as the roll pack thins. Further, the difference in separation force curves between Schedules A and B should be noted; Schedule A is in three steps and Schedule B is serrated due to the difference in reheat frequency. Roll-separation force is clearly observed to decrease every time the roll pack is reheated, which correlates well to the measured values for force.

Simulations were also conducted for Schedule A using U-10Mo mechanical properties obtained from compression tests performed at PNNL and reported by Joshi et al. [23,24]. Fig. 7 represents a comparison between measured rolled separating force, and model predictions using properties from the literature (Simulated Separation Force 1) and from PNNL compression tests (Simulated Separation Force 2). Taking into account the material work-hardening for temperatures below 550 °C was reflected on the simulated roll-separating force, which is in a better agreement with the measurements. We can clearly observe the shift to the top of the roll-separating force curve after introducing the work-hardening observed in compression tests. Note that the predicted forces using PNNL compression data deviate less than 3% over the entire rolling schedule, whereas the predicted forces using literature data deviate ~7% from the measurements.

4.2. Thickness variation and dog-boning

Achieving a uniform thickness of U-10Mo foil is a major objective of this rolling process. A closer look at the simulation results revealed the presence of localized thickening (dog-boning) at both ends of the U-10Mo sheet within the 1018 can. To quantify the observed dog-boning in the simulations, the thickness variation along the centerline of the U-Mo sheet for both Schedules A and B was plotted in Fig. 8. Thickness is measured at 50 equidistant points from one end of the coupon to the other, along the mid-plane of the alloy coupon lengthwise. Dog bone areas show an ~25 and 23% thickness increase with respect to the average thickness in the remaining part of the coupon for Schedules A and B, respectively.

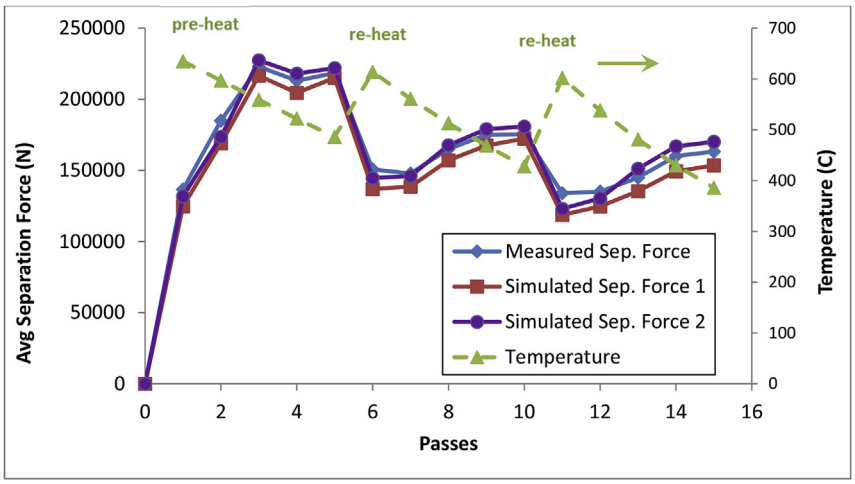

Fig. 7. Measured separation forces compared to simulated separation forces (using mechanical properties from 1) the literature and 2) PNNL compression tests) for the first 15 passes of Schedule A.

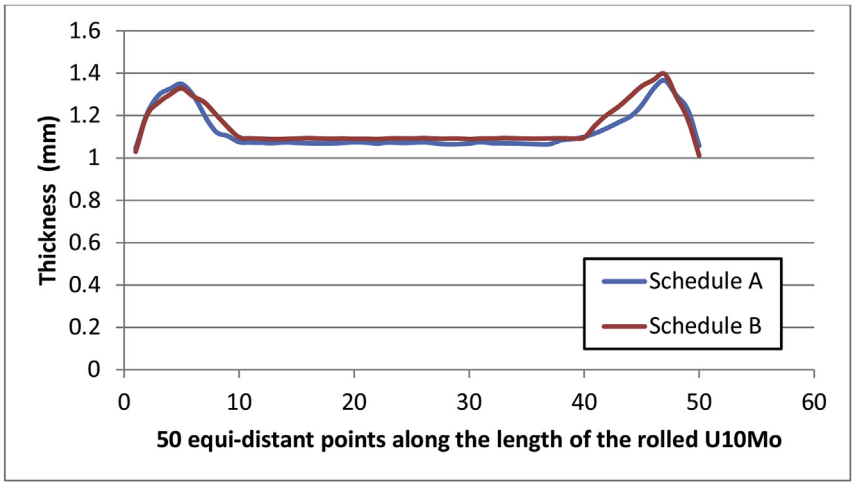

Fig. 8. Thickness variation along the coupon for Schedules A and B.

Dog-boning is considered one of the major issues of rolling a fuel coupon inside a picture-frame type of can and has been observed in actual rolled U-Mo fuels. This highly undesirable effect likely results from the difference in yield strength between the 1018 steel material (can) and the U-10Mo (fuel coupon). Dog-boning occurs when the sheet pack first enters the rolls and the separation force is entirely a result of rolling the 1018 can. As the U-10Mo enters the roll pinch zone, it only makes up a small fraction of the material being rolled. As the 1018 pulls, via friction, the U-10Mo into the rolls, a gap begins to form between the 1018 can and the U-Mo sheet. The harder U-Mo acts as a non-deformable mandrel and the 1018 flows past the U-10Mo, forming a gap between the can and the U-Mo as observed in the FEM (see Fig. 9). Once the tension and roll pinching is sufficient to pull the U-Mo into the rolls, the 1018 can has been thinned and the U-Mo rolls to a thicker dimension forming the thick end of the dog bone. As the U-Mo is rolled, the entire 1018 can is pulled into the rolls and the U-Mo becomes thinner.

Pedrosa et al. [16] observed both waviness and dog-boning in their experiment on the hot co-rolling of U-10Mo monolithic fuel in zircaloy cladding. Dog-boning was present in rolled samples at all temperatures ranging from 650 °C to 950 °C. This dog-boning also

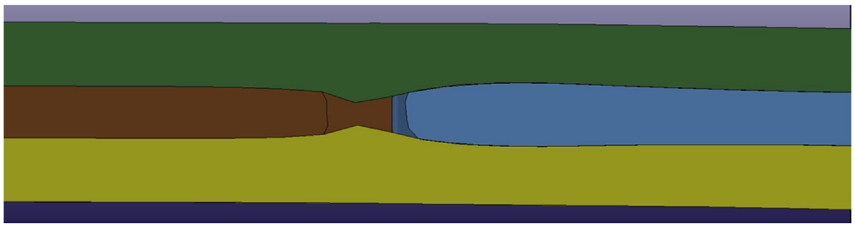

Fig. 9. Gap formed between the end of the U-Mo coupon and the 1018 can.

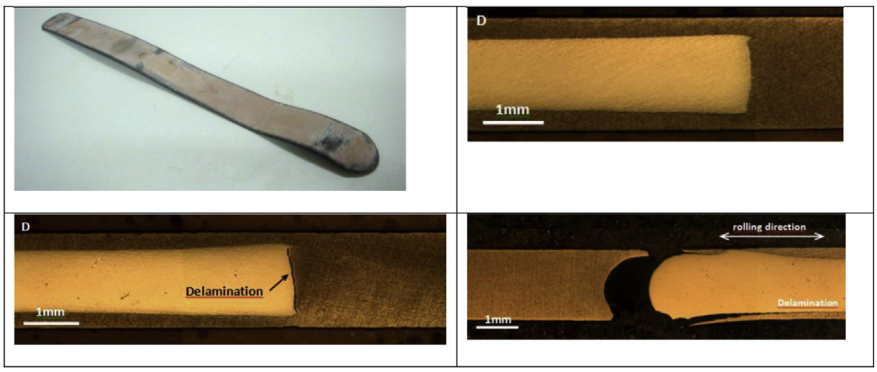

Fig. 10. Hot co-rolled U-10Mo in zircaloy clad from Ref. [19].

caused delamination at the ends of the monolithic fuel in the dog-boning area as seen in Fig. 10.

A different combination of materials, with less yield strength differential between the fuel and the can, might be an efficient way of reducing dog-boning. The FEM simulation, using a rigid non-distorting roll stand may overpredict the dog-boning; however, dog-boning was observed in all co-rolled U-10Mo sheet packs. This non-uniformity results in the need for trimming to ensure uniform thickness, and an associated yield loss.

Because rolling defects, such as dog-boning, waviness, and thickness non-uniformity, were observed in the simulation predictions for both schedules, a parametric study of the influence of the cladding material on the rolling defects was conducted following the rolling Schedule A presented in previous sections.

4.3. Influence of the can material on dog-boning

Four cases were considered in this parametric study: 1) rolling of a U-10Mo coupon inside a 1018 steel can, 2) rolling of a U-10Mo coupon inside a 304 stainless steel can, 3) rolling of a U-10Mo coupon inside a Zircaloy-2 can, and 4) bare rolling of a U-10Mo coupon. To quantify the observed dog-boning in the simulations, the thickness variation along the centerline of the U-10Mo sheet was plotted in Fig. 11. Thickness is measured at 50 equidistant points from one end of the coupon to the other, along the mid-plane of the alloy coupon lengthwise. Dog-bone areas show a ~25% thickness increase with respect to the average thickness in the remaining part of the coupon for the 1018 steel can. About a 19% increase in thickness is observed in the case of rolling inside the 304 stainless steel can, whereas only ~15% increase in thickness at the edges of the U-10Mo coupon is observed in the case of rolling inside a Zircaloy-2 can. The bare rolling case does not show any dog-boning and we can observe a relatively uniform thickness along the coupon. Dog-boning amplitude is inversely proportional to the strength of the can material. In fact, the stronger the can material, the less likely localized thickening of the fuel alloy and thinning of the cladding at the edges of the fuel core will be observed.

Fig. 12 represents the gap between the U-10Mo coupon and the picture-frame can material for 1018 steel and Zircaloy-2 can rolling. Note that this gap is larger for “softer” can materials like 1018 carbon steel and thus leads to more thinning of the clad, hence more thickening of the fuel core. Using Zircaloy-2 as a can material reduces the amplitude of dog-boning by ~40%, whereas 304 stainless steel represents an intermediate solution to the dog-boning issue. Another way of quantifying dog-boning is to represent the roll-separation force before, during, and after the pinch zone at the extremity of the fuel core.

Thickness variation was also monitored along the width of the rolled sheet. Except for the areas near the edges where dog-boning was observed, the thickness is uniform along the width of the U-10Mo coupons. Fig. 13 shows an isometric view, with a cross section in the middle along the width, of the rolled sheet after 10 passes in the case of the Zircaloy-2 can. Dog-boning near the edge

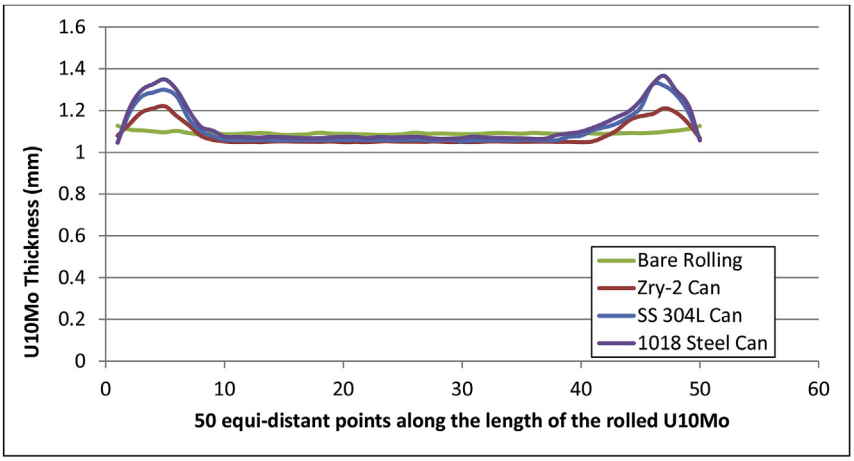

Fig. 11. Thickness variation across the length of the U-10Mo coupon in the cases of 1) rolling inside 1018 steel can, 2) rolling inside 304 stainless steel can, 3) rolling inside Zircaloy-2 can, and 4) bare rolling.

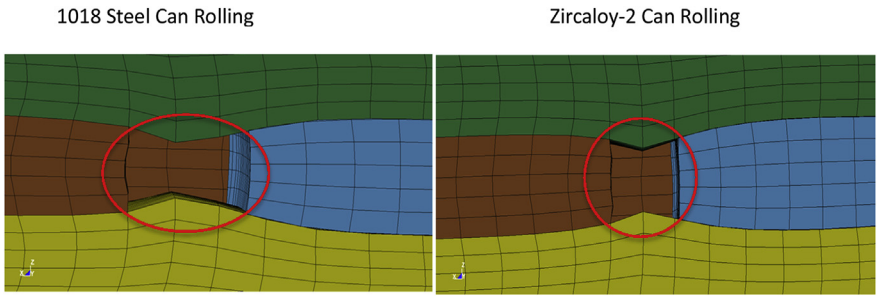

Fig. 12. Gap between the U-10Mo coupon and the picture-frame can material for 1018 steel and Zircaloy-2 can rolling.

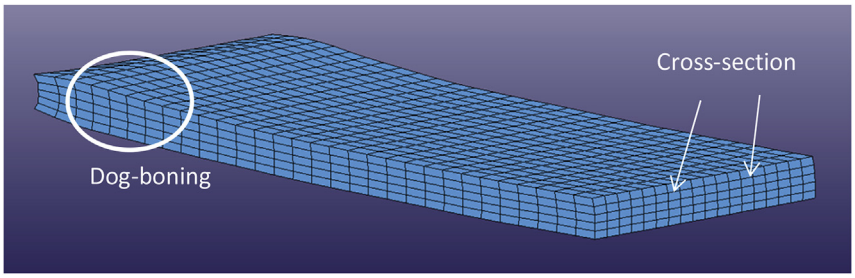

Fig. 13. Isometric view of the U-10Mo coupon, cross-sectioned in the middle widthwise, after 10 passes in the case of the Zircaloy-2 can.

lengthwise is clearly observed, but the thickness does not vary much along the width. Generally, variation in thickness across the width of the rolled sheet is caused by the deformation of the rolls. Because we are modeling the rolls as rigid bodies, no roll flattening or roll bending under load is allowed.

4.4. Influence of the can material on waviness

Waviness of the rolled sheet pack is also observed in canned fuel rolling. This waviness was measured and is represented in Fig. 14 comparing coupons rolled inside a 1018 steel can, inside a Zircaloy-2 can, and rolled bare. The picture in the plot represents a longitudinal cross section of the U-10Mo coupon along the middle line. Point #1 is located at the left bottom corner of the cross section. Vertical distances between point #1 and point # {2 …13}, all located at the bottom surface of the alloy coupon, have been measured and values are reported on the plot. Waviness is more pronounced in the case of 1018 can rolling compared to 304 stainless steel can and Zircaloy-2 can rolling, whereas almost no waviness is present in the bare-rolling case. In general, this defect can result from various aspects of the rolling process, including bending of the rolls, variation of the roll-separation force along the sheet, dog-boning, etc. As stated before, because no deformation of the rolls is present in our modeling approach, we only focus on waviness causes other than bending and flattening of the rolls. The gap between the fuel core and the can picture frame appears to be the major contributor to this defect. This gap results from the mismatch of strength between the U-10Mo coupon and the can material. A sudden change in the material resistance, when the rolls reach the fuel core, leads to an increase in the roll-separation force and therefore to the initiation of the waviness of the sheet. Fig. 14 also shows the relatively uniform bare-rolled U-10Mo coupon, where no dog-boning, waviness, and thickness variation in any direction are observed in the predicted bare-rolled sheet.

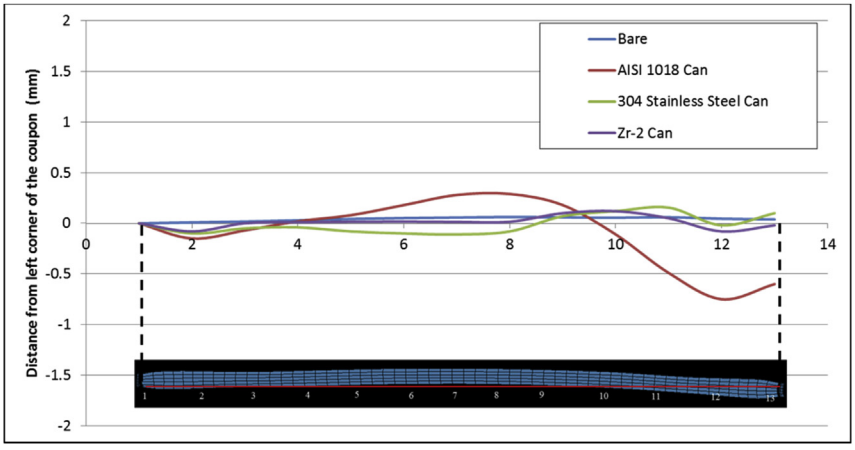

Fig. 14. Representation of the waviness of the U-10Mo coupon.

5. Conclusions

- A finite-element model of the pack-rolling process of U-10Mo canned in 1018 steel was produced and shown to correlate well to experimental roll-separation forces and pack thickness observed in actual rolling operations.
- Two rolling schedules were simulated; one that used 2 reheats in 15 passes and one that used 7 reheats in 15 passes. The predicted force and thickness for the two-reheat pass deviated less than 7% from the measured values. The seven-reheat schedule showed a steadily increasing overprediction of the separation force to a maximum variation of 14%. The close correlation with early passes of Schedule A and the entire two-reheat schedule indicates that the increased time and temperature may result in a change in the microstructure of the U-10Mo or 1018 steel. This change in mechanical behavior with time at temperature has not been investigated and is not accounted for in the constitutive relations for either U-10Mo or 1018 steel.
- The finite-element model of the pack-rolling process was used to explain a geometric non-uniformity commonly found in pack rolled sheets known as dog-boning. This results in reduced yield of uniform sheet and has been attributed to a mismatch in flow stress of the 1018 steel and the U-10Mo at the ends of the roll pack.
- Various cladding material cases were simulated and results show that a can material with a flow stress that more closely matches that of U-10Mo reduces dog-boning and waviness. In fact rolling simulations using Zr-2 can show a significant improvement of the waviness and dog-boning as compared to mild steel can.

Acknowledgements

The current work was supported by U.S. Department of Energy, National Nuclear Security Administration (NNSA) under Contract DE-AC05-76RL01830. Roll-separation force data were obtained from experiments conducted at the Idaho National Laboratory in 2008. The authors acknowledge those who were involved with the experiments and collection of the raw data, including Mr. Glenn Moore, Mr. Blair Park, Mrs. Francine Rice, and Mr. Steve Steffler. The authors appreciate the opportunity to use the roll-separation force data to validate the model presented here.

References

[1] J.L. Snelgrove, G.L. Hofman, M.K. Meyer, C.L. Trybus, T.C. Wiencek, Development of very-high-density low-enriched-uranium fuels, Nucl. Eng. Des. 178 (1997) 119–126.
[2] D.B. Lee, K.H. Kim, C.K. Kim, Thermal compatibility studies of unirradiated U-Mo alloys dispersed in aluminum, J. Nucl. Mater 250 (1997) 79–82.
[3] J.M. Park, K.H. Kim, C.K. Kim, M.K. Meyer, G.L. Hofman, R.V. Strain, The irradiation behavior of atomized U-Mo alloy fuels at high temperature, J. Met. Mater Int. 7 (2) (2001) 151–157.
[4] M.K. Meyer, G.L. Hofman, S.L. Hayes, C.R. Clark, T.C. Wienceck, J.L. Snelgrove, R.V. Strain, K.H. Kim, Low-temperature irradiation behavior of uranium-molydenum alloy dispersion fuel, J. Nucl. Mater. 304 (2002) 221–236.
[5] H. Ozaltun, M.H.H. Shen, P. Medvedev, Assessment of residual stresses on U10Mo alloy based monolithic mini-plates during hot isostatic pressing, J. Nucl. Mater. 419 (1–3) (2011) 76–84.
[6] X. Kong, H. Yang, S. Ding, Zircaloy plate rolling simulation with an effective strain-rate-dependent stress-updating algorithm, J. Non. Sci. Num. Sim 17 (2) (2016) 113–125.
[7] J.-F. Jue, B. Park, C. Clark, G. Moore, D. Keiser Jr., Fabrication of monolithic rertr fuels by hot isostatic pressing, Nucl. Technol. 172 (2) (2010) 204–210.
[8] Y. Hwu, J.G. Lenard, A finite element study of flat rolling, Trans. ASME J. Eng. Mater. Tech. 110 (1988) 22–26.
[9] R.I. Nepershin, Plane strain hot rolling of slab and strip, Int. J. Mech. Sci. (1999) 1401–1421.
[10] M.R. Shuai, Q.X. Huang, Y.C. Zhu, Finite element simulation of the hot-rolling process of titanium alloy bar, Adv. Mater. Res. 145 (2010) 181–186.
[11] A.K. Tieu, Z.Y. Jiang, C. Lu, A 3D finite element analysis of the hot rolling of strip with lubrication, J. Mater. Process. Technol. 125–126 (2002) 638–644.
[12] C.W. Knight, S.J. Hardy, A.W. Lees, K.J. Brown, Influence of roll speed mismatch on strip curvature during the roughing stages of a hot rolling mill, J. Mater. Process. Technol. 168 (1) (2005) 184–188.
[13] LS-Dyna, User's Manual - Livermore Software Technology Corporation, Livermore CA, 2015.
[14] A. Soulami, C.A. Lavender, D.M. Paxton, D. Burkes, Rolling Process Modeling Report: Finite-element Prediction of Roll Separating Force and Rolling Defects, PNNL-23313, Pacific Northwest National Laboratory, Richland, WA, 2014.
[15] A. Soulami, C.A. Lavender, D.M. Paxton, D. Burkes, Rolling Process Modeling Report: Finite-Element Model Validation And Parametric Study On Various Rolling Process Parameters, PNNL-24362, Pacific Northwest National Laboratory, Richland, WA, 2015.
[16] F. Seredynski, Prediction of plate cooling during rolling-mill operation, J. Iron Steel Inst (1973) 197–203.
[17] B. Avitzur, Handbook of Metal-Forming Processes, Willey-Interscience, 1982.
[18] W. Thurber, R. Beaver, Development of Silicon-modified 48 wt % U-Al, ORNL-2602, Oak Ridge Natlional Laboratory, 1959.
[19] T. Pedrosa, J.G. Brina, J. Bosco de Paula, F. Lameiras, W. Ferraz, Preliminary results for the co-rolling process fabrication of plate-type nuclear fuel based in U-10Mo monolithic meat and zircaloy-4 cladding, in: International Nuclear Atlantic Conference - INAC Recife, Brazil, 2013.
[20] E.E. Pasqualini, Monolithic UMo nuclear fuel plates with non aluminium cladding, in: RRFM2008 Transactions, Session 2: Fuel Development and Fabrication, Hamburg, Germany, 2008, pp. 123–127.
[21] D.E. Burkes, C.A. Papesch, A.P. Maddison, T. Hartmann, F.J. Rice, Thermophysical proerties of DU-10 wt.% Mo alloys, J. Nucl. Mater. 403 (2010) 160–166.
[22] D.E. Burkes, T. Hartmann, R. Prabhakaran, J.-F. Jue, Microstructural characteristics of Du-xMo alloys with x = 7-12wt%, J. Alloys Compd. 479 (2009) 140–147.
[23] V.V. Joshi, E.A. Nyberg, C.A. Lavender, D. Paxton, H. Garmestani, D.E. Burkes, Thermomechanical process optimization of U-10 wt% Mo – Part 1: high-temperature compressive properties and microstructure, J. Nucl. Mater. 465 (2015) 805–813.
[24] V.V. Joshi, E.A. Nyberg, C.A. Lavender, D. Paxton, D.E. Burkes, Thermomechanical process optimization of U-10wt% Mo – Part 2: the effect of homogenization on the mechanical properties and microstructure, J. Nucl. Mater. 465 (2015) 710–718.
[25] F. Seredynski, Prediction of plate cooling during rolling-mill operation, J. Iron Steel Inst (1973) 197–203.
[26] B. McPherson, The Determination of True Stress – True Strain Curves and Modulus of Elasticity of a Uranium – 10 w/o Molybdenum Alloy at Elevated Temperatures, AECU-3801, 1958.
[27] M.S. Farkas, Mechanical and Physical Properties of Fuels and Cladding Materials with Potential for Use in Brookhaven's Pulsed Fast Reactor, Part I, BMI-X-455, 1967.
[28] M.B. Waldron, R.C. Burnett, S.F. Pugh, The Mechanical Properties of Uranium-molybdenum Alloys, AERE-M/R-2554, 1958.
[29] AN-176, Final Report on Conceptual Design and Initial Radiological Safety Study for a Pulsed Nuclear Reactor, 1960.
[30] C.A.W. Peterson, R.R. Vandervoort, Stress-cracking in the Uranium-10 w/o Molybdenum Alloy, University of California Lawrence Radiation Laboratory Report UCRL-7767, 1964.
[31] T.L.G.H.E. Boyer, in: OH (Ed.), Metals Handbook, Materials Park, American Society for Metals, 1985.
[32] C.L. Whitmarsh, Review of Zircaloy-2 and Zircaloy-4 Properties Relevant to N. S. Savannah Reatcor Design, seventeenth ed., Oak Ridge National Laboratory, ORNL-3281, UC-80-Reactor Technology, TID-4500, 1962.
[33] J. Chen, B. Young, Stress-strain curves for stainless steel at elevated temperatures, Eng. Struct. 28 (2) (2006) 229–239.
[34] S. Chavez, G.E. Korth, D.M. Harper, T.J. Walker, High-temperature tensile and creep data for Inconel 600, 304 stainless steel, and SA106B Carbon steel, Nucl. Eng. Des. 148 (2–3) (1994) 351–363.
[35] F.J. Clauss, Engineer's Guide to High-temperature Materials, Addison-Wesley, 1969.
[36] G.A. Moore, M.C. Marshall, Co-rolled U10Mo/Zirconium-barrier-layer Monolithic Fuel Foil Fabrication Process, INL Report, INL/EXT-10–17774, 2010.

Abbreviations

DOE: U.S. Department of Energy
FEM: finite-element modeling
HEU: high-enriched uranium
LEU: low-enriched uranium
NNSA: National Nuclear Security Administration
PNNL: Pacific Northwest National Laboratory
U-10Mo: uranium alloyed with 10 wt% molybdenum
UTS: ultimate tensile stress
YS: yield stress